Enhanced Polarization Locking in VCSELs

Zifeng Yuan,[1] Dewen Zhang,[1] Lei Shi,[1] Yutong Liu,[1] and Aaron Danner[1]
National University of Singapore, Department of Electrical and Computer Engineering, Singapore

(*Electronic mail: adanner@nus.edu.sg)

(Dated: 5 August 2026)

While optical injection locking (OIL) of vertical-cavity surface-emitting lasers (VCSELs) has been widely studied in the past, the polarization dynamics of OIL have received far less attention. Recent studies suggest that polarization locking via OIL could enable novel computational applications such as polarization-encoded Ising computers. However, the inherent polarization preference and limited polarization switchability of VCSELs hinder their use for such purposes. To address these challenges, we fabricate VCSELs with tailored oxide aperture designs and combine these with bias current tuning to study the overall impact on polarization locking. Experimental results demonstrate that this approach reduces the required injection power (to as low as 3.6 μW) and expands the locking range. To investigate the impact of the approach, the spin-flip model (SFM) is used to analyze the effects of amplitude anisotropy and bias current on polarization locking, demonstrating strong coherence with experimental results.

arXiv:2604.01857v2 [physics.optics] 4 Aug 2026

Optical injection locking (OIL) is a technique that synchronizes a slave laser (SL) to a master laser (ML) by injecting light from the ML into the SL's cavity, enabling the SL to lase at the same frequency, polarization, and with a fixed phase offset to the ML. OIL has been widely applied in diverse fields such as optical communications[1–6], optical frequency comb generation[7–10], arbitrarily shaped optical pulse generation[11,12], and even frequency locking in quantum teleportation[13,14]. Vertical-cavity surface-emitting lasers (VCSELs) have emerged as widely used semiconductor lasers in OIL due to their compact footprint, low power consumption, and ease of integration into large-scale arrays[15–19].

Research specifically focusing on polarization locking via OIL has received limited attention and has not typically been a primary focus. However, recent studies suggest that polarization locking of VCSELs holds significant potential for novel computational applications, such as polarization-encoded Ising computers and optical neural networks[20–31], where encoding bits or qubits into orthogonal lasing polarization states presents a promising approach. What many of these applications require is a VCSEL that exhibits equal preference for two orthogonal polarization states[20,21,26]. In other words, an ideal VCSEL for these applications should exhibit easily switchable (unstable) polarization states, which are better suited for achieving polarization locking. However, typically VCSELs inherently exhibit gain anisotropy caused by strain or crystal anisotropy, resulting in a polarization state with predominantly higher gain[32]. This characteristic presents challenges for polarization locking: for VCSELs with strong anisotropy, the polarization state becomes fixed and resistant to switching, or achieving polarization locking requires a high injection power[21,26].

Various approaches have been explored to achieve polarization control and to investigate polarization switching or its suppression in VCSELs[33–58]. Among these, several methods have been introduced to control anisotropic gain[33,34,37–41], including tailoring the aperture shape[40,41]. Other approaches involve anisotropic current injection mechanisms[42] and optical injection locking[43,44]. Additionally, polarization control has been demonstrated using surface gratings[45–47], liquid crystals[48–50], and metasurface integration[51–55]. Many of these studies have shown that polarization switching occurs when gain anisotropy or amplitude anisotropy is reduced, leading to polarization instability in VCSELs.

To enhance the polarization locking performance of VCSELs, this work builds upon prior studies[40,41] that leverage aperture engineering to control polarization properties. We fabricate VCSELs with tailored aperture structures to control amplitude anisotropy, specifically VCSELs which yield less anisotropy in polarization than is typical, thereby improving polarization switchability. Furthermore, we evaluate the OIL performance of these VCSELs under different bias currents. The paper is structured as follows: first, we detail the experimental setup and methods. This is followed by experimental results and comparison with the state-of-the-art in OIL, supported by spin-flip model (SFM) simulations, which illustrate how amplitude anisotropy and bias current influence polarization locking.

The configuration of our experimental setup is shown in Fig. 1(a). It begins with collimated light from the VCSEL ML, emitting light with a center wavelength tunable from 835.57 nm to 841.47 nm, controlled by a temperature controller and a laser diode controller. The spectrum of the emitted light is illustrated in Fig. 1(c). The injection power is modulated by rotating two linear polarizers (LP1 and LP2), while a half-wave plate (HWP) or quarter-wave plate (QWP) is used to adjust the polarization state of the ML light. The light is then directed through a 50:50 beam splitter (BS1), with half sent to a port that employs a power meter for monitoring the injection power, or a polarimeter (Thorlabs, PAX1000IR1) for measuring the state of polarization of collimated input light using the rotating-wave-plate method, providing azimuth and ellipticity, or an optical spectrum analyzer (OSA) for measuring the spectrum of the ML light. The other half of the beam continues through another 50:50 beam splitter (BS2) and is directed into the fabricated VCSELs on the chip, serving as the SLs. Accurate focusing of the ML light onto the SL's cavity is achieved using a 20×NIR MO and an XY piezo stage. Current is supplied to the SL chip via probing. The output light from the SL passes through BS2 and BS1, ultimately reaching a port used to measure the output power, polarization state, or spectrum of the SL light. To ensure that parasitic light from

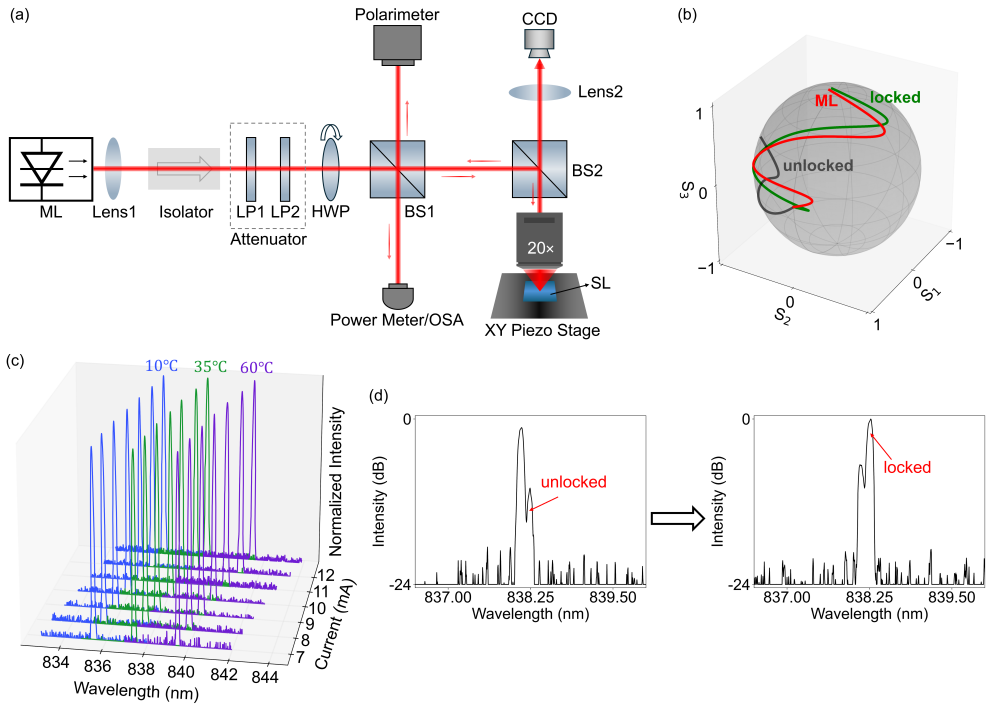


FIG. 1. (a) Experimental schematic illustrating the free-space OIL setup. ML: master laser, SL: slave laser, LP: linear polarizer, HWP: half-wave plate, BS: beam splitter, OSA: optical spectrum analyzer. (b) Poincaré sphere showing the polarization states of the ML, the SL unlocked and locked. (c) Spectral of the ML under varying operating conditions. (d) Spectral of the SL in the unlocked and locked states. The peak intensity has been shifted to 0 dB.

the ML does not affect the polarimeter measurements, we first turn off the SL while keeping the ML on. The optical power detected at the polarimeter port is measured and found to be negligible.

An example of polarization locking outcomes is illustrated in Fig. 1(b) and Fig. 1(d), based on the results from the setup shown in Fig. 1(a). Some details such as bias current, frequency detuning and injection power, are further explored in this study. As shown in Fig. 1(b), the SL's polarization state aligns with the ML under sufficient injection power (locked condition), while it deviates from the ML when the injection power is insufficient (unlocked condition). Fig. 1(d) depicts the SL spectrum under locked and unlocked conditions, with both panels sharing the same normalized power scale. In the left panel (unlocked), with no ML injection, the dominant peak corresponds to the SL's natural polarization state. The goal is to lock the second-highest peak, which has an orthogonal polarization state. To achieve this, the ML's polarization is adjusted to be orthogonal to the SL's natural state, and its wavelength is tuned to align with the second-highest peak. In the right panel (locked), sufficient injection power from the ML causes this target peak to become dominant, while the first peak is suppressed.

In this study, our objective is to enhance the OIL performance, aiming to reduce the injection power required for polarization locking and to expand the locking range. First, we fabricate seven aperture designs, corresponding to Fig. 2(a)–(g) in the following order: square, cruciform (1:0.7 aspect ratio), cruciform (1:0.7 aspect ratio) rotated by 30°, 60°, and 90°, and cruciform (1:0.6 aspect ratio) without and with 90° rotation. The epitaxial wafer used to fabricate VCSELs consists of a GaAs (100) substrate, 40 pairs of bottom Si:GaAs distributed Bragg reflectors (DBRs), GaAs quantum wells, and 28 pairs of top C:GaAs DBRs, with a high-Al oxide layer embedded within the top DBRs. The rotation angle is defined as the angle between the longer arm of the cruciform aperture and the primary flat of a (100) GaAs wafer, which we define as the horizontal direction. First, a backside n-type contact (AuGe/Ni/Au) is deposited via electron beam evaporation. The top p-type contacts are then defined using photolithography, followed by Ti/Pt/Au evaporation and lift-off. To form mesas, a SiO_2 hard mask is deposited via plasma-enhanced chemical vapor deposition (PECVD), followed by photolithography and subsequent etching of unprotected SiO_2 with buffered oxide etch (BOE). The mesa structures are then formed using dry etching via inductively coupled plasma (ICP). After mesa etching, The high-Al layer undergoes wet oxidation at 450°C, with the oxidation rate precisely controlled at 0.1 μm/min by adjusting the N_2 flow rate and water steam temperature.

These tailored aperture structures influence the amplitude anisotropy along two orthogonal directions (horizontal and vertical), which in turn determines the polarization state and its switching properties under increasing bias currents. The corresponding switching properties are illustrated in the light power output versus current (LI) curves, measured at room

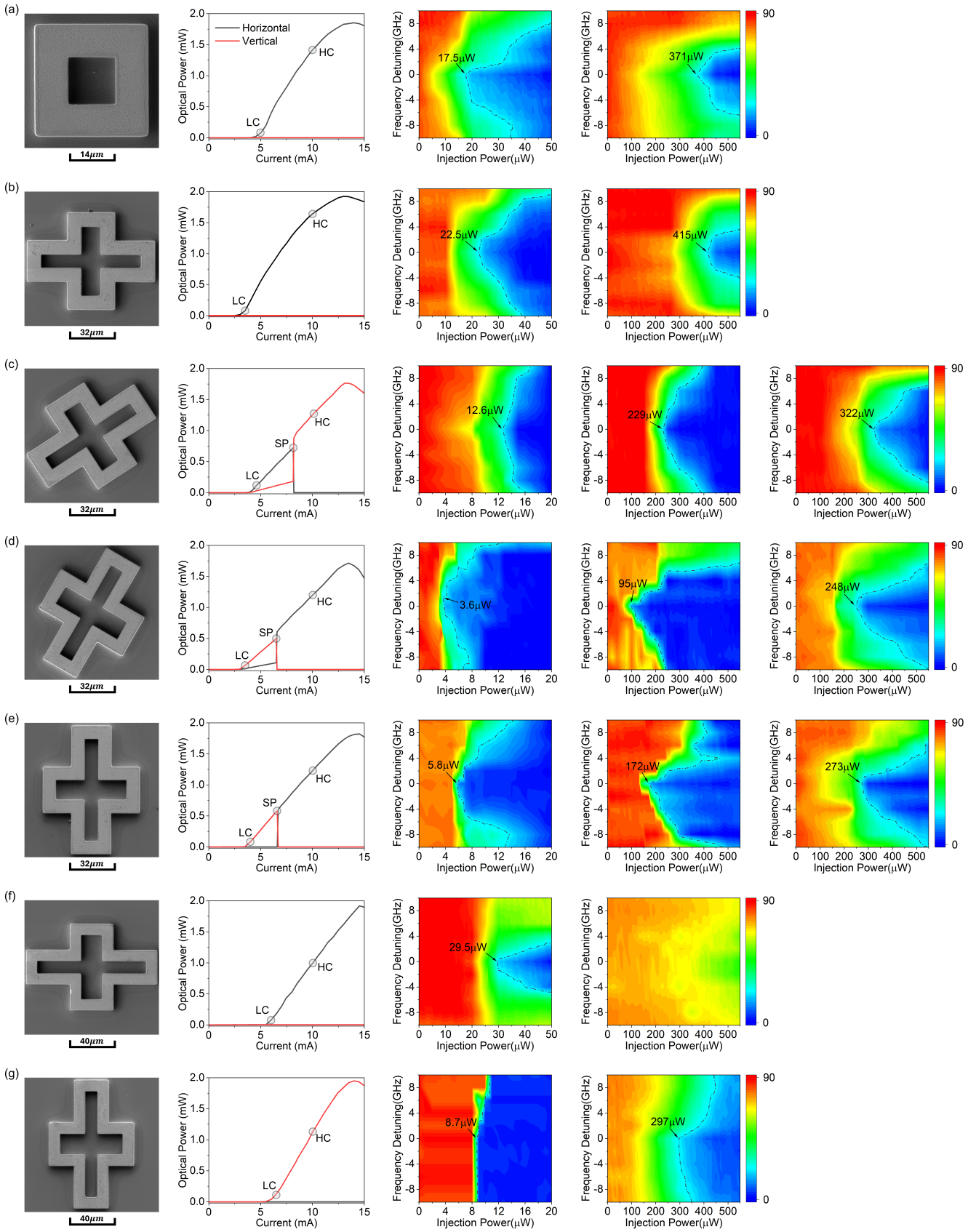


FIG. 2. OIL performance for VCSELs with tailored aperture designs. (a)–(g) correspond to: (a) square aperture; (b)–(e) cruciform aperture (1:0.7 aspect ratio, rotated by 0°, 30°, 60°, and 90°); (f)–(g) cruciform aperture (1:0.6 aspect ratio, without and with 90° rotation). The first column shows scanning electron microscope images, the second column presents LI curves for horizontal and vertical polarizations, and the remaining columns display locking diagrams at low current (LC), switching point (SP, omitted for non-switchable VCSELs), and high current (HC). The locking diagrams illustrate the absolute polarization difference, $\Delta\theta = |\theta_{\mathrm{SL}} - \theta_{\mathrm{ML}}|$, where θ_{SL} and θ_{ML} are the absolute azimuths of SL and ML measured by the polarimeter. A dashed line indicates the boundary between unlocked and locked states. The minimum injection power required for successful polarization locking is highlighted.

TABLE I. Summary of OIL performance from some recent papers (2000 to present).

Year	Minimum injection power	Locking range	Wavelength (nm)	SL Laser type	Ref.
···	3.6 μW	$\Delta f = (-10, +10)$ GHz	838.25	VCSEL	This work
2024	2.5 μW	$\Delta f = -12.46$ GHz*	850	VCSEL	26
2023	94 μW	$\Delta f = -23.58$ GHz*	976.77	VCSEL	59
2023	−19 dB	$\Delta f = (0, +30)$ GHz	1547	VCSEL	60
2017	25.1 μW*	$\Delta f = +0.5$ GHz*	1540	VCSEL	12
2017	11 μW*	···	850	VCSEL	61
2017	∼ 1 μW*	$\Delta f = (-8, -2), (0, +2)$ GHz*	1540.91	VCSEL	62
2017	3.16 μW	···	1550	VCSEL	63
2017	10 dB*	$\Delta f = -1.01$ GHz*	1542.4	VCSEL	64
2016	0.8 mW*	$\Delta f = -12.46$ GHz*	850	VCSEL	65
2016	2 mW	$\Delta f = (-19.37, -12.91)$ GHz*	681.72–682.12	VCSEL	66
2016	10 mW*	$\Delta f = -63.06$ GHz*	1542.35	VCSEL	67
2016	17.23 mW*	···	1537.95	VCSEL	68
2014	50 μW	$\Delta f = (-2.45, +1.55)$ GHz	1538.01–1538.24	VCSEL	69
2013	···	$\Delta f = (-20, +15)$ GHz	1550	VCSEL	70
2011	26.9 μW	$\Delta f = (-12, +8)$ GHz	1550	VCSEL	71
2011	1 mW	$\Delta f = (-10, 0)$ GHz	850	VCSEL	72
2011	···	$\Delta f = (-9, +2)$ GHz	1550	VCSEL	73
2009	3.981 mW	$\Delta f = (-15.9, +26.98)$ GHz*	1300	VCSEL	74
2008	7.9 μW	$\Delta f = (-12.64, +12.64)$ GHz*	1540.3	VCSEL	75
2008	< 63 mW*	$\Delta f = (-47, +67)$ GHz	1550	VCSEL	76
2007	< 25 μW*	···	1550	VCSEL	77
2006	13.2 μW	$\Delta f = (-84, -4), (+50, +76)$ GHz*	850	VCSEL	78
2003	30 μW	$\Delta f = (-18.73, -2.5)$ GHz*	1550	VCSEL	2
2024	1 μW	$\Delta f = (-1.799, +1.195)$ GHz	1549.315	Edge(DFB)	9
2024	3.16 μW	$\Delta f = +9.40$ GHz	1552.6	Edge(DFB)	79
2024	20 nW	$\Delta f = +0.62$ GHz	1550	Edge(DFB)	80
2024	1 μW*	$\Delta f = (0, +6)$ GHz*	1575.4	Edge(DFB)	81
2024	1 mW*	$\Delta f = -50$ GHz*	1550	Edge(DFB)	82
2024	−12 dB	$\Delta f = (-15, +5)$ GHz	···	Edge(DFB)	6
2022	−45 dB*	$\Delta f = (0, +4.55)$ GHz*	1550	Edge(DFB)	83
2022	···	$\Delta f = (+12.07, +25.37)$ GHz	1556	Edge(DFB)	84
2022	1 μW	$\Delta f = +35$ MHz	1550	Edge(DFB)	14
2018	0.316 nW	$\Delta f = +10$ GHz	1550	Edge(DFB)	85
2015	1 μW	$\Delta f = (-0.5, +0.5)$ GHz	1550	Edge(DFB)	8
2011	1 mW	$\Delta f = (-0.5, +0.5)$ GHz*	1566	Edge(DFB)	86
2022	−15 dB	···	1302	Edge(FP)	10
2018	2 mW	$\Delta f = +10$ GHz	1556	Edge(FP)	87
2016	300 μW	···	399	Edge(FP)	88
2016	500 μW	$\Delta f = (-2.5, +2.5)$ GHz	461	Edge(FP)	89
2012	63.1 μW	$\Delta f = (-36.8, +36.8)$ GHz*	1563.22	Edge(FP)	90
2022	−27 dB	$\Delta f = (-0.12, +0.12)$ GHz	1550	InP-Si_3N_4 lasers	5
2008	28 mW	···	1550	Erbium-Doped Fiber Laser	91
2006	···	$\Delta f = (-7, +7)$ MHz	1064	Nd:YVO4 Laser	92

Edge (FP): Fabry-Pérot edge-emitting lasers; Edge (DFB): distributed-feedback edge-emitting lasers.
* Calculated or estimated using other information provided in the respective papers.

temperature with a current bias ranging from 0 to 15 mA, as shown in Fig. 2. Here, "Horizontal" refers to the dominant polarization direction in square-aperture VCSELs, which is naturally aligned with the primary flat of a (100) GaAs wafer. The polarimeter is calibrated accordingly to ensure that measured polarization states are consistently referenced across all devices. "Vertical" corresponds to the orthogonal direction, and these definitions serve as fixed reference points for all polarization measurements.

To illustrate the impact of aperture engineering on OIL, we

focus on the role of built-in gain anisotropy on the polarization state. On our wafer, the VCSELs inherently exhibit higher gain anisotropy in the horizontal polarization state. For example, in Fig. 2(a), square apertures are geometrically symmetric along the horizontal and vertical orthogonal directions. However, due to the inherent gain anisotropy, the horizontal polarization state becomes dominant, and no polarization switching occurs as the bias current increases, as shown in the LI curve in Fig. 2(a). By modifying the aperture shapes, such as using cruciform designs, we can either strengthen (e.g., Fig. 2(b), with a ratio of 1:0.7 and a longer horizontal arm) or mitigate (e.g., Fig. 2(e), with a ratio of 1:0.7 rotated by 90°, where the vertical arm is longer) the built-in amplitude anisotropy. For instance, in cruciform (ratio 1:0.7) rotated by 90°, the natural horizontal anisotropy is suppressed, resulting in a less stable polarization state that is easier to switch with increasing injection current, as shown in the LI curve in Fig. 2(e). Conversely, greater anisotropy leads to more stable polarization states that are harder to switch, as observed in the LI curve in Fig. 2(b).

Next, we bias the current at three distinct levels to evaluate its impact on OIL performance of each VCSEL: low current (LC), just above the threshold current; the switching point (SP), where polarization switching occurs for part of the fabricated VCSELs; and high current (HC), fixed at 10 mA for all VCSELs. The corresponding OIL performance is presented in the locking maps on the right in Fig 2. From left to right, the maps sequentially present the performance for LC, SP (omitted for unswitchable VCSELs), and HC.

We evaluate the OIL performance of all the fabricated VCSELs in our optical setup by varying the injection power and frequency detuning between the ML and the SL within the range of ± 10 GHz. In this setup, the polarization state of the ML is adjusted to be orthogonal to the SL. The results show that VCSELs exhibiting polarization switching properties (Fig. 2(c)–(e)) have better OIL performance. At the same bias current (10 mA at HC), the minimum injection power required for these switchable VCSELs is 248 μW, as shown in Fig. 2(d). In contrast, non-switchable VCSELs, such as Fig. 2(a), require a higher minimum injection power of 371 μW. Additionally, the locking range (indicated by the blue area) is broader for switchable VCSELs compared to non-switchable ones. By lowering the bias current from HC to LC, the minimum injection power can be further reduced from 248 μW to 3.6 μW (Fig. 2(d)).

This work achieves a relatively low minimum injection power when compared to other reports of injection-locked VCSELs. Although not absolutely the lowest, the method provides a complementary approach to further enhance OIL performance limits. A detailed comparison of OIL performance of various lasers in recent years, including VCSELs, Fabry-Pérot edge-emitting lasers (Edge(FP)), distributed-feedback edge-emitting lasers (Edge(DFB)), and others, is presented in Table 1. Among these, Edge(DFB) lasers achieve the lowest minimum injection power; however, their locking range is narrower compared to VCSELs. Our method simultaneously achieves low injection power over a wide locking range.

To investigate, from a theoretical standpoint, how the proposed method influence VCSEL OIL performance, we employ the SFM[36,70,73], which considers spin sublevels of the conduction and valence bands in quantum well lasers. Spin-up (n^+) and spin-down (n^-) electron recombination generate two lasing transitions: right and left circularly polarized states ($\tilde{E}_+$ and $\tilde{E}_-$). These transitions are coupled through the total carrier density $N=(n^+ + n^-)/2$ and the spin carrier density difference $m=(n^+ - n^-)/2$. These field components can be rewritten in terms of x- and y-polarization states. The rate equations for an optically injected VCSEL are expressed as follows:

$$\begin{aligned}
\frac{dE_x}{dt} &= \kappa[(N-1)E_x - mE_y(\sin\Delta\phi + \alpha\cos\Delta\phi)] \\
&\quad -\gamma_a E_x + K_{\text{inj}} E_{\text{injx}}\cos\Delta_x, \qquad (1)\\
\frac{dE_y}{dt} &= \kappa[(N-1)E_y + mE_x(\alpha\cos\Delta\phi - \sin\Delta\phi)] \\
&\quad +\gamma_a E_y + K_{\text{inj}} E_{\text{injy}}\cos\Delta_y, \qquad (2)\\
\frac{d\phi_x}{dt} &= \kappa\left[\alpha(N-1) + m\frac{E_y}{E_x}(\cos\Delta\phi - \alpha\sin\Delta\phi)\right] \\
&\quad -\Delta\omega - \alpha\gamma_a + K_{\text{inj}}\frac{E_{\text{injx}}}{E_x}\sin\Delta_x, \qquad (3)\\
\frac{d\phi_y}{dt} &= \kappa\left[\alpha(N-1) - m\frac{E_x}{E_y}(\alpha\sin\Delta\phi + \cos\Delta\phi)\right] \\
&\quad -\Delta\omega + \alpha\gamma_a + K_{\text{inj}}\frac{E_{\text{injy}}}{E_y}\sin\Delta_y, \qquad (4)\\
\frac{dN}{dt} &= -\gamma\left[N\left(1+E_x^2+E_y^2\right) - \eta - 2mE_yE_x\sin\Delta\phi\right], \qquad (5)\\
\frac{dm}{dt} &= -\gamma_s m - \gamma\left[m\left(E_x^2+E_y^2\right)\right] + 2\gamma N E_y E_x\sin\Delta\phi. \qquad (6)
\end{aligned}$$

TABLE II. SFM parameters.

Symbol	Value	
γ_a	0 / −30	GHz
γ_s	50	GHz
γ_p	2	GHz
γ	1	GHz
η	[1.1, 3.4]	
κ	300	GHz
α	3	
K_{inj}	35.5	GHz

The parameters used in our SFM are summarized in Table 2, with values adjusted from our previous work to simulate an 850 nm VCSEL[21]. Here, κ represents the cavity decay rate related to photon lifetime, while γ represents the decay rate of the total carrier population. The parameter α is known as the linewidth enhancement factor. γ_s accounts for the population differences between spin-up and spin-down states. η represents the electrical pumping term. The gain anisotropy can be split into amplitude and phase terms, represented by γ_a and γ_p, respectively. γ_a, influenced by factors such as anisotropic quantum well gain and cavity geometry, is the key parameter targeted for control in the first method, while γ_p affects the resonance frequency. These two components are typically treated as independent factors[36]. The two linearly polarized

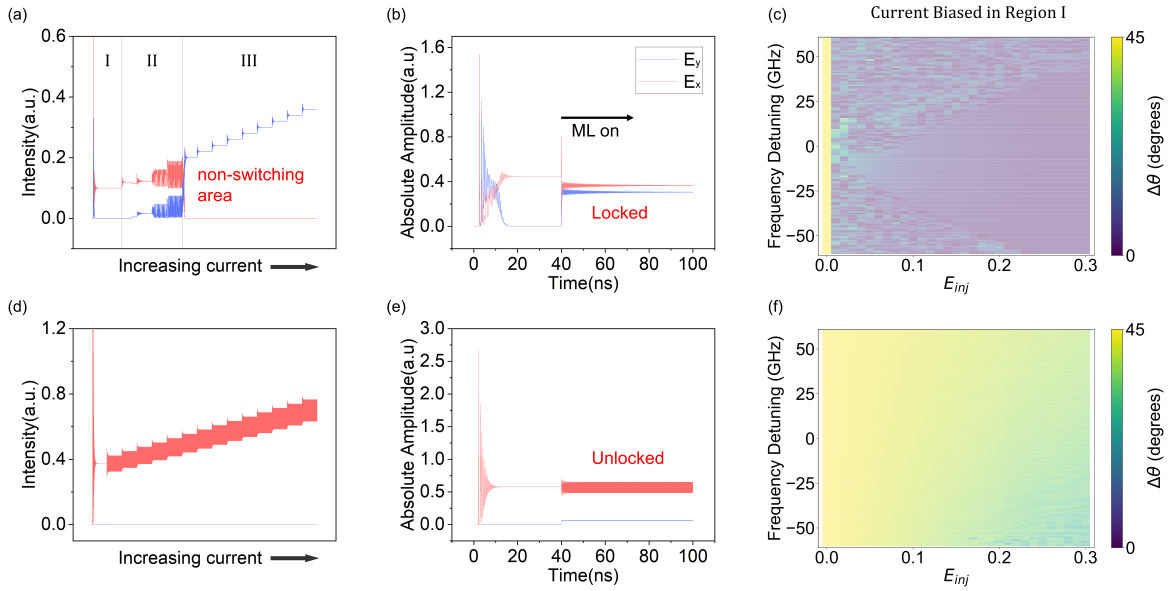


FIG. 3. VCSEL polarization dynamics under different amplitude anisotropy conditions: (a)–(c) for $\gamma_a = 0$ and (d)–(f) for $\gamma_a = -30$ GHz. (a), (d) Evolution of polarization states of a solitary VCSEL with increasing electrical pumping term (η). For $\gamma_a = 0$, the polarization switches from x-dominant (black curve) to y-dominant (red curve) as η increases, while for $\gamma_a = -30$ GHz, the polarization remains x-dominant. (b), (e) Both VCSELs are biased at $\eta = 1.1$, and the ML emits linearly polarized light at 45° injected into the SL at $t = 40$ ns. (c), (f) Locking maps showing $\Delta\theta = |\theta_{\mathrm{SL}} - \theta_{\mathrm{ML}}|$ for varying E_{inj} and frequency detuning ($\Delta\omega$) at $\eta = 1.1$.

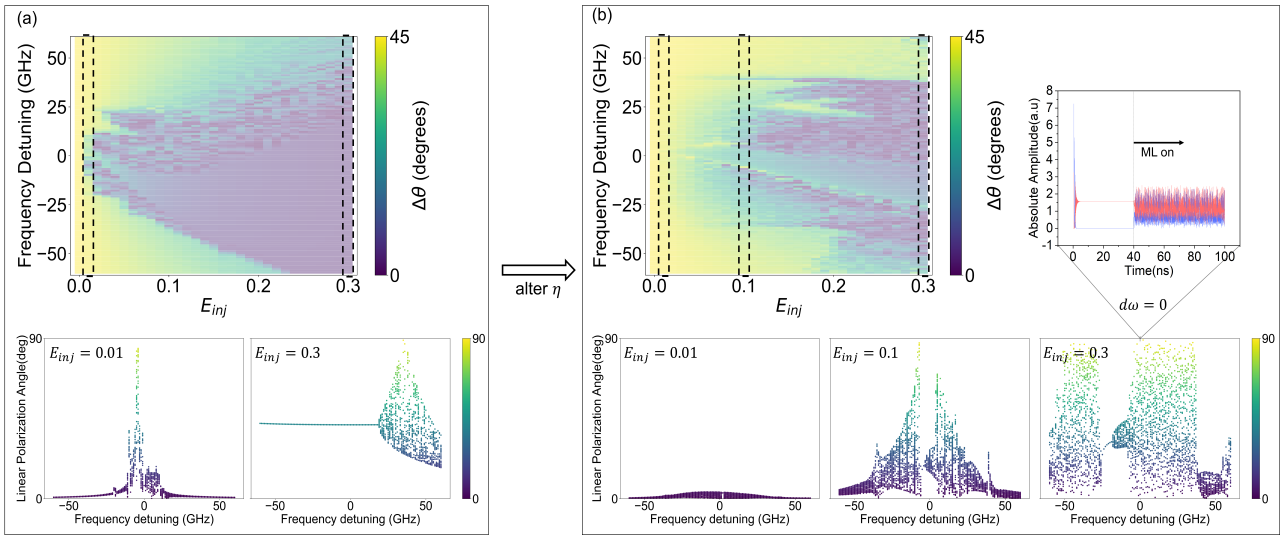


FIG. 4. VCSEL OIL performance under different bias current conditions for $\gamma_a = 0$, with locking maps shown at $\eta = 1.2$ (a) and $\eta = 3.4$ (b). Below the locking maps, the linear polarization angles of the SLs under OIL are shown for certain E_{inj} values, corresponding to the black-boxed regions in the locking maps. At $\eta = 3.4$, the polarization dynamic of the VCSEL under OIL with $E_{\mathrm{inj}} = 0.3$ and $\Delta\omega = 0$ is illustrated in the top-right inset of (b).

modes have resonance frequencies given by $\omega_x = \alpha\gamma_a - \gamma_p$ and $\omega_y = \gamma_p - \alpha\gamma_a$, respectively. The magnitudes of $\Delta\phi$, Δ_x, and Δ_y are given by $\Delta\phi = 2(\gamma_p - \alpha\gamma_a)t + \phi_y - \phi_x$, $\Delta_x = \omega_y t - \phi_x$, and $\Delta_y = \omega_x t - \phi_y$.

The ML output is set to emit linearly polarized light at 45°, with amplitude along the x- and y-directions set as $E_{\mathrm{injx}} = E_{\mathrm{injy}} = E_{\mathrm{inj}}$, and the coupling coefficient is denoted as K_{inj}. In this simulation, the value of E_{inj} varies from 0 to 0.3. The frequency detuning ($\Delta\omega$), defined as the difference between the ML and SL frequencies, is swept from −60 GHz to +60 GHz. For each value set of E_{inj} and $\Delta\omega$, 100 simulations are conducted. For each value set, the average polarization difference ($\Delta\theta = |\theta_{\mathrm{SL}} - \theta_{\mathrm{ML}}|$) at $t = 100$ ns is calculated.

In the above experiments, modifying the arm length ratio of the cruciform or rotating its angle alters the amplitude anisotropy (γ_a) along two orthogonal directions. For a soli-

tary VCSEL with $\gamma_a = 0$ (Fig. 3(a)), polarization switching occurs with increasing injection current, whereas with strong γ_a (Fig. 3(d)), the polarization state remains stable and does not switch. When the current is biased at the same level ($\eta = 1.1$, corresponding to Region I) and the ML is injected, VCSELs with $\gamma_a = 0$ (Fig. 3(b)) achieve polarization locking, as indicated by the predominance of purple regions in the locking map (Fig. 3(c)). In contrast, for VCSELs with strong γ_a (Fig. 3(e)), the polarization state remains unlocked, as indicated by the yellow regions in the locking map (Fig. 3(f)). When γ_a is too strong, the gain in one direction far exceeds that in the orthogonal direction, allowing the inherent gain to dominate over the external photon injection.

Next, we set $\gamma_a = 0$ to isolate its impact and adjust the electrical pumping to $\eta = 1.2$ (the switching point between Region II and Region III) and $\eta = 3.4$ (Region III). The corresponding locking maps are shown in Fig. 4(a) and Fig. 4(b), respectively. As η increases from 1.2 to 3.4, the locking range becomes narrower, and the minimum E_{inj} required to achieve locking increases. These changes suggest that higher bias currents make OIL more difficult, as the system requires stronger external injection to compensate for the reduced locking range.

For both current bias points, the locking range expands as E_{inj} increases. Below the locking diagrams, the linear polarization angle of the SL under OIL is shown for specific values of E_{inj}, corresponding to the black-boxed regions in the locking maps, visualizing the results of all 100 runs for each frequency detuning value. For $\eta = 1.2$, two cases are highlighted: $E_{\text{inj}} = 0.01$ and $E_{\text{inj}} = 0.3$. At $E_{\text{inj}} = 0.01$, the SL is influenced by the ML only near zero frequency detuning. Increasing E_{inj} to 0.3 extends the locking range, the SL remains stably locked at 45° for most $\Delta\omega$ values, with instability observed only for a small range of positive detuning. When η is increased to 3.4, the SL initially remains unaffected by the ML at $E_{\text{inj}} = 0.01$. As E_{inj} increases from 0.01 to 0.3, the locking range expands, with the polarization state of the SL being influenced by the ML across more frequency detuning values. The top-right inset in Fig. 4(b) zooms in on the case where $E_{\text{inj}} = 0.3$ and $\Delta\omega = 0$. Here, the SL's polarization state starts oscillating between two orthogonal states after the ML is turned on. This locking behavior is less stable compared to cases with lower η.

In summary, we first fabricate VCSELs with tailored aperture designs to control amplitude anisotropy. Then, we optimize the bias current to investigate its role in enhancing polarization locking. We achieve a minimum injection power of 3.6 μW and robust polarization locking across a frequency detuning range of $\pm$10 GHz. The low minimum injection power and expanded locking range lower the difficulty of polarization locking, enhancing the potential for polarization encoding in optical computing applications, such as VCSEL-based Ising computers and optical neural networks[20–26,93]. Moreover, in large-scale Ising computers, where numerous VCSELs share the same injection power, achieving polarization locking with the reduced injection power allocated to each VCSEL becomes a critical challenge[26], highlighting the importance of designing systems that facilitate polarization locking with ease. These improvements may further support emerging applications in computational imaging[94,95] and machine learning[96–102].

ACKNOWLEDGMENTS

This work was supported by the National Research Foundation, Singapore, under its Competitive Research Programme (NRF CRP24-2020-0003) and by both the National Research Foundation, Singapore, and A*STAR under the Quantum Engineering Programme (NRF 2021-QEP2-02-P12).

CONFLICT OF INTEREST

The authors have no conflicts to disclose.

DATA AVAILABILITY

The data that support the findings of this study are available from the corresponding author upon reasonable request.

REFERENCES

[1] K. Kikuchi, T. Okoshi, M. Nagamatsu, and N. Henmi. Degradation of bit-error rate in coherent optical communications due to spectral spread of the transmitter and the local oscillator. *J. Lightw. Technol.*, 2(6):1024–1033, 1984.
[2] C. H. Chang, L. Chrostowski, and C. J. Chang-Hasnain. Injection locking of VCSELs. *IEEE J. Sel. Top. Quantum Electron.*, 9(5):1386–1393, 2003.
[3] Z. Liu, J.-Y. Kim, D. S. Wu, et al. Homodyne ofdm with optical injection locking for carrier recovery. *J. Lightw. Technol.*, 33(1):34–41, 2014.
[4] K. Kasai, Y. Wang, S. Beppu, et al. 80 gbit/s, 256 qam coherent transmission over 150 km with an injection-locked homodyne receiver. *Opt. Express*, 23(22):29174–29183, 2015.
[5] L. Gonzalez-Guerrero, R. Guzman, M. Ali, et al. Injection locking properties of a dual laser source for mm-wave communications. *J. Lightw. Technol.*, 40(20):6685–6692, 2022.
[6] Arbnor Berisha, Hendrik Boerma, Ronald Kaiser, et al. Minimizing noise in distributed reflector laser types under optical injection locking. *IEEE J. Quantum Electron.*, 60(4):1–6, 2024.
[7] E. Temprana, E. Myslivets, B.-P. Kuo, et al. Transmitter-side digital back propagation with optical injection-locked frequency-referenced carriers. *J. Lightw. Technol.*, 34(15):3544–3549, 2016.
[8] R. Zhou, T. Shao, M. D. G. Pascual, et al. Injection-locked wavelength demultiplexer for optical comb-based nyquist wdm system. *IEEE Photon. Technol. Lett.*, 27(24):2595–2598, 2015.
[9] Weihao Li, Lulu Chen, Yuqi Li, et al. Unlocking dscm-based self-homodyne coherent multiple access through comb distribution and optical injection locking. *J. Lightw. Technol.*, 43:2492–2502, 2024.
[10] Jia-Jian Chen, Wen-Qi Wei, Jia-Le Qin, et al. Multi-wavelength injection locked semiconductor comb laser. *Photon. Res.*, 10:1840–1847, 2022.
[11] D. S. Wu, D. J. Richardson, and R. Slavík. Optical fourier synthesis of high-repetition-rate pulses. *Optica*, 2(1):18–26, 2015.
[12] S. P. Bhooplapur, A. Klee, and P. J. Delfyett. Line-by-line pulse-shaping at ghz modulation frequencies with an injection-locked VCSEL array. *IEEE Photon. Technol. Lett.*, 29(15):1241–1244, 2017.
[13] T. K. Paraïso, I. De Marco, T. Roger, et al. A modulator-free quantum key distribution transmitter chip. *NPJ Quantum Information*, 5(1):42, 2019.

[14]Zikang Su, Dajian Cai, Hao Jiang, et al. Optical injection locking based local oscillator regeneration for continuous variable quantum key distribution. *Opt. Lett.*, 47:1287–1290, 2022.

[15]K. Iga. Surface emitting laser—its birth and generation of new optoelectronics field. *IEEE J. Sel. Top. Quantum Electron.*, 6:1201, 2000.

[16]P. Moser, J. A. Lott, and D. Bimberg. Energy efficiency of directly modulated oxide-confined high bit rate 850-nm VCSELs for optical interconnects. *IEEE J. Sel. Top. Quantum Electron.*, 19:1702212, 2013.

[17]K. Hirose, Y. Liang, Y. Kurosaka, et al. Watt-class high-power, high-beam-quality photonic crystal lasers. *Nat. Photonics.*, 8:406–411, 2014.

[18]A. J. Danner, J. J. Rafery, P. O. Leisher, and K. D. Choquette. Single mode photonic crystal vertical cavity lasers. *Appl. Phys. Lett.*, 88:1114, 2006.

[19]T. Heuser, M. Pflüger, I. Fischer, et al. Developing a photonic hardware platform for brain-inspired computing based on 5×5 VCSEL arrays. *J. Phys. Photonics*, 2(4):044002, 2020.

[20]S. Utsunomiya, K. Takata, and Y. Yamamoto. Mapping of ising models onto injection-locked laser systems. *Opt. Express*, 19(19):18091–18108, 2011.

[21]B. Loke, Z. Yuan, S. T. Lim, and A. Danner. Linear polarization state encoding for Ising computing with optically injection-locked VCSELs. *Journal of Optical Microsystems*, 4(1):014501, 2024. doi:10.1117/1.JOM.4.1.014501.

[22]M. Babaeian, D. T. Nguyen, V. Demir, et al. A single shot coherent ising machine based on a network of injection-locked multicore fiber lasers. *Nat. Commun.*, 10(1):3516, 2019.

[23]Y. Gao, G. Chen, L. Qi, W. Fu, Z. Yuan, and A. J. Danner. Photonic Ising machines for combinatorial optimization problems. *Applied Physics Reviews*, 11(4):041307, 2024. doi:10.1063/5.0216656.

[24]Z. Chen, A. Sludds, R. Davis III, et al. Deep learning with coherent VCSEL neural networks. *Nat. Photonics.*, 17(8):723–730, 2023.

[25]Y. Lan, G. Chen, Y. Gao, et al. An integrated all-optical ising machine with unlimited spin array size and coupling. *Adv. Photon. Res.*, 5:2400004, 2024.

[26]D. Zhang, Z. Yuan, T. X. Hoang, W. Fu, C. E. Png, S. T. Lim, and A. Danner. All-optical scalable and programmable VCSEL-based Ising annealer with parallel feedback. *Optics Express*, 33(11):22119–22131, 2025. doi:10.1364/OE.546402.

[27]S. T. Lim, D. Zhang, Z. Yuan, T. X. Hoang, C. E. Png, and A. Danner. Quantum-inspired VCSEL-based optical parallel feedback system for large-scale combinatorial optimization. In *2024 IEEE Opto-Electronics and Communications Conference (OECC)*, pages 1–3, Melbourne, Australia, 2024. doi:10.1109/OECC54135.2024.10975547.

[28]S. T. Lim, T. Y. L. Ang, Z. Yuan, T. X. Hoang, D. Zhang, C. E. Png, A. J. Danner, and G. Alagappan. Advancing detector shielding with thermo-optic defocusing in PMMA integrated on silicon nitride. In *Proceedings of the International Conference on Photonics, Optics and Laser Technology (PHOTOPTICS)*, pages 92–94, 2025.

[29]D. Zhang, Z. Yuan, T. X. Hoang, C. E. Png, S. T. Lim, and A. Danner. A VCSEL-based optical Ising computer with parallel feedback system for large-scale optimization. In *CLEO: Applications and Technology*, Technical Digest Series, page JPS200_182. Optica Publishing Group, 2025.

[30]D. Zhang, Z. Yuan, A. J. Danner, S. T. Lim, and T. X. Hoang. VCSEL-based all-optical Ising machine, 2025. US Patent Application 19/068,345.

[31]Z. Yuan, T. Chen, D. Zhang, Y. Gao, W. Shan, B. Lin, and A. Danner. Tailored polarization-switchable VCSEL arrays for photonic Ising computing. *Applied Physics Letters*, 127(22):221102, 2025. doi:10.1063/5.0291349.

[32]S. Gehrsitz, F. K. Reinhart, C. Gourgon, et al. The refractive index of $Al_xGa_{1-x}As$ below the band gap: Accurate determination and empirical modeling. *J. Appl. Phys.*, 87(11):7825–7837, 2000.

[33]C. J. Chang-Hasnain, J. P. Harbison, G. Hasnain, et al. Dynamic, polarization, and transverse mode characteristics of vertical cavity surface emitting lasers. *IEEE J. Quantum Electron.*, 27(6):1402–1409, 1991.

[34]K. D. Choquette, K. L. Lear, R. E. Leibenguth, et al. Polarization modulation of cruciform vertical-cavity laser diodes. *Appl. Phys. Lett.*, 64(21):2767–2769, 1994.

[35]G. Verschaffelt, K. Panajotov, J. Albert, et al. Polarisation switching in vertical-cavity surface-emitting lasers: from experimental observations to applications. *Opto-Electron. Rev.*, 9(3):257–268, 2001.

[36]J. Martin-Regalado, F. Prati, and M. San Miguel. Polarization properties of vertical-cavity surface-emitting lasers. *IEEE J. Quantum Electron.*, 33(5):765–783, 1997.

[37]A. K. Jansen van Doorn, M. P. Van Exter, and J. P. Woerdman. Elasto-optic anisotropy and polarization orientation of vertical-cavity surface-emitting semiconductor lasers. *Appl. Phys. Lett.*, 69(8):1041–1043, 1996.

[38]K. Panajotov, B. Nagler, G. Verschaffelt, et al. Impact of in-plane anisotropic strain on the polarization behavior of vertical cavity surface-emitting lasers. *Appl. Phys. Lett.*, 77:1590, 2000.

[39]K. Panajotov, J. Danckaert, G. Verschaffelt, et al. Polarization behavior of vertical-cavity surface-emitting lasers: Experiments, models and applications. In *AIP Conference Proceedings*, volume 560, pages 403–417. American Institute of Physics, 2001.

[40]K. D. Choquette and R. E. Leibenguth. Control of vertical-cavity laser polarization with anisotropic transverse cavity geometries. *IEEE Photonics Technol. Lett.*, 6:40, 1994.

[41]K. Panajotov, M. Camarena, M. C. Moreno, et al. Polarization behavior and mode structure of vertical-cavity surface-emitting lasers with elliptical surface relief. In *Proc. SPIE*, volume 4994, page 127, 2003.

[42]M. P. Tan, A. M. Kasten, T. A. Strand, et al. Polarization switching in vertical-cavity surface-emitting lasers with anisotropic cavity geometry and injection. *IEEE Photonics Technol. Lett.*, 24(9):745–747, 2012.

[43]S. Hallstein, J. D. Berger, M. Hilpert, et al. Manifestation of coherent spin precession in stimulated semiconductor emission dynamics. *Phys. Rev. B*, 56(12):R7076, 1997.

[44]S. Iba, S. Koh, K. Ikeda, et al. Room temperature circularly polarized lasing in an optically spin injected vertical-cavity surface-emitting laser with (110) gaas quantum wells. *Appl. Phys. Lett.*, 98(8), 2011.

[45]J. M. Ostermann, P. Debernardi, C. Jalics, et al. Surface gratings for polarization control of single-and multi-mode oxide-confined vertical-cavity surface-emitting lasers. *Opt. Commun.*, 246(4–6):511–519, 2005.

[46]M. C. Y. Huang, Y. Zhou, C. J. Chang-Hasnain, et al. A surface-emitting laser incorporating a high-index-contrast subwavelength grating. *Nat. Photonics*, 1(2):119–122, 2007.

[47]C. J. Chang-Hasnain and W. Yang. High-contrast gratings for integrated optoelectronics. *Adv. Opt. Photon.*, 4:379–440, 2012.

[48]V. I. Kopp, Z. Q. Zhang, and A. Z. Genack. Lasing in chiral photonic structures. *Prog. Quantum Electron.*, 27(6):369–416, 2003.

[49]I. J. Hodgkinson, M. Arnold, M. W. McCall, et al. Chiral mirror and optical resonator designs for circularly polarized light: suppression of cross-polarized reflectances and transmittances. *Opt. Commun.*, 210(3–6):201–211, 2002.

[50]V. I. Kopp, B. Fan, H. K. M. Vithana, et al. Low-threshold lasing at the edge of a photonic stop band in cholesteric liquid crystals. *Opt. Lett.*, 23(21):1707–1709, 1998.

[51]X. Jia, J. Kapraun, J. Wang, et al. Metasurface reflector enables room-temperature circularly polarized emission from vcsel. *Optica*, 10(8):1093–1099, 2023.

[52]Y. Y. Xie, P. N. Ni, Q. H. Wang, et al. Metasurface-integrated vertical cavity surface-emitting lasers for programmable directional lasing emissions. *Nat. Nanotechnol.*, 15(2):125–130, 2020.

[53]D. Wen and K. B. Crozier. Metasurfaces 2.0: Laser-integrated and with vector field control. *APL Photonics*, 6(9), 2021.

[54]K. Li, Y. Rao, C. Chase, et al. Monolithic high-contrast metastructure for beam-shaping vcsels. *Optica*, 5(1):10–13, 2018.

[55]M. S. Seghilani, M. Myara, M. Sellahi, et al. Vortex laser based on iii-v semiconductor metasurface: direct generation of coherent laguerre-gauss modes carrying controlled orbital angular momentum. *Sci. Rep.*, 6(1), 2016.

[56]Z. Yuan, D. Zhang, H. Lin, and A. Danner. Engineering polarization switching in VCSELs with custom aperture shapes. In *CLEO: Science and Innovations*, Technical Digest Series, page JPS200_47. Optica Publishing Group, 2025.

[57]Z. Yuan, D. Zhang, Y. Gao, L. Qi, W. Fu, and A. Danner. Large-scale fabrication and analysis of polarization behavior in VCSELs with tailored apertures. *Journal of Lightwave Technology*, 43(14):6819–6827, 2025. doi:10.1109/JLT.2025.3568130.

[58]Z. Yuan, W. Shan, T. Chen, B. Lin, and A. Danner. Mesa orientation engineering for polarization locking in VCSELs. In *2025 IEEE Photonics Conference (IPC)*, pages 1–2, Singapore, Singapore, 2025.

doi:10.1109/IPC65510.2025.11282171.

[59] M. Pflüger, D. Brunner, T. Heuser, et al. Injection locking and coupling the emitters of large VCSEL arrays via diffraction in an external cavity. *Opt. Express*, 31(5):8704–8713, 2023.

[60] N. Yokota, K. Ikeda, and H. Yasaka. Observation of spin polarization modulation responses of injection-locked vertical-cavity surface-emitting lasers. *IEICE Electron. Express*, 20(8):20230057–20230057, 2023.

[61] S. Nazhan and Z. Ghassemlooy. Polarization switching dependence of VCSEL on variable polarization optical feedback. *IEEE J. Quantum Electron.*, 53(4):1–7, 2017.

[62] F. Denis le Coarer, A. Quirce, P. Pérez, et al. Injection locking and polarization switching bistability in a 1550 nm VCSEL subject to parallel optical injection. *IEEE J. Sel. Top. Quantum Electron.*, 23(6):1–10, 2017.

[63] J. Jignesh, B. Corcoran, J. Schröder, et al. Polarization independent optical injection locking for carrier recovery in optical communication systems. *Opt. Express*, 25(18):21216–21228, 2017.

[64] X. Xiao, N. K. Fontaine, H. Chen, et al. High-speed iq modulator based on injection-locked VCSEL array. In *CLEO: Science and Innovations*, page STu1M.6. Optica Publishing Group, 2017.

[65] H. H. Lu, C. Y. Li, H. W. Chen, et al. 45 gb/s pam4 transmission based on VCSEL with light injection and optoelectronic feedback techniques. *Opt. Lett.*, 41(21):5023–5026, 2016.

[66] H. H. Lu, C. Y. Li, H. W. Chen, et al. A 56 gb/s pam4 VCSEL-based lifi transmission with two-stage injection-locked technique. *IEEE Photon. J.*, 9(1):1–8, 2016.

[67] N. K. Fontaine, X. Xiao, H. Chen, et al. Chirp-free modulator using injection locked VCSEL phase array. In *ECOC 2016 - Post Deadline Paper; 42nd European Conference on Optical Communication*, pages 1–3. VDE, 2016.

[68] E. Prior, C. De Dios, R. Criado, et al. Dynamics of dual-polarization VCSEL-based optical frequency combs under optical injection locking. *Opt. Lett.*, 41(17):4083–4086, 2016.

[69] H. Lin, P. Pérez, A. Valle, et al. Investigation of elliptically polarized injection locked states in VCSELs subject to orthogonal optical injection. *Opt. Express*, 22(5):4880–4885, 2014.

[70] R. Al-Seyab, K. Schires, A. Hurtado, et al. Dynamics of VCSELs subject to optical injection of arbitrary polarization. *IEEE J. Sel. Top. Quantum Electron.*, 19(4):1700512, 2013.

[71] P. Pérez, A. Quirce, L. Pesquera, et al. Polarization-resolved nonlinear dynamics induced by orthogonal optical injection in long-wavelength VCSELs. *IEEE J. Sel. Top. Quantum Electron.*, 17(5):1228–1235, 2011.

[72] A. A. Qader, Y. Hong, and K. A. Shore. Lasing characteristics of VCSELs subject to circularly polarized optical injection. *J. Lightw. Technol.*, 29(24):3804–3809, 2011.

[73] R. Al-Seyab, K. Schires, N. A. Khan, et al. Dynamics of polarized optical injection in 1550-nm VCSELs: Theory and experiments. *IEEE J. Sel. Top. Quantum Electron.*, 17(5):1242–1249, 2011.

[74] A. Hayat, A. Bacou, A. Rissons, et al. Long wavelength VCSEL-by-VCSEL optical injection locking. *IEEE Trans. Microw. Theory Tech.*, 57(7):1850–1858, 2009.

[75] K. H. Jeong, K. H. Kim, S. H. Lee, et al. Optical injection-induced polarization switching dynamics in 1.5-μm wavelength single-mode vertical-cavity surface-emitting lasers. *IEEE Photon. Technol. Lett.*, 20(10):779–781, 2008.

[76] E. K. Lau, X. Zhao, H. K. Sung, et al. Strong optical injection-locked semiconductor lasers demonstrating > 100-ghz resonance frequencies and 80-ghz intrinsic bandwidths. *Opt. Express*, 16(9):6609–6618, 2008.

[77] X. Zhao, D. Parekh, E. K. Lau, et al. Novel cascaded injection-locked 1.55-μm VCSELs with 66 ghz modulation bandwidth. *Opt. Express*, 15(22):14810–14816, 2007.

[78] I. Gatare, M. Sciamanna, J. Buesa, et al. Nonlinear dynamics accompanying polarization switching in vertical-cavity surface-emitting lasers with orthogonal optical injection. *Appl. Phys. Lett.*, 88(10), 2006.

[79] Mingzhao Chen, Yin Xu, Zhexin Zhang, et al. Stabilized brillouin laser with sub-hz fundamental linewidth aided by frequency shifted optical injection locking. *APL Photonics*, 9(2):026103, 2024.

[80] Zhuo-Yue Wen, Fan Yang, Zhencan Yang, et al. Spectrally efficient photonic terahertz transmitter for kramers-kronig reception without guardband based on optical injection locking. *J. Lightw. Technol.*, 42(16):5466–5475, 2024.

[81] Siyu Luo, Zhengxuan Li, Bingyao Cao, et al. Optical carrier regeneration based on injection locking for single-sideband self-coherent detection. *Opt. Express*, 32:46415–46427, 2024.

[82] Y. Liu, Y. Zhang, S. Guan, et al. Modulation bandwidth enhancement and chirp reduction in integrated optical injection locking dfb laser. *IEEE J. Quantum Electron.*, 2024.

[83] Daniel J. Herrera, Vassilios Kovanis, and Luke F. Lester. Using transitional points in the optical injection locking behavior of a semiconductor laser to extract its dimensionless operating parameters. *IEEE J. Sel. Top. Quantum Electron.*, 28(1: Semiconductor Lasers):1–9, 2022.

[84] G. Lihachev, W. Weng, J. Liu, et al. Platicon microcomb generation using laser self-injection locking. *Nat. Commun.*, 13:1771, 2022.

[85] R. Kakarla, J. Schröder, and P. A. Andrekson. Optical injection locking at sub nano-watt powers. *Opt. Lett.*, 43(23):5769–5772, 2018.

[86] M. J. Fice, A. Chiuchiarelli, E. Ciaramella, et al. Homodyne coherent optical receiver using an optical injection phase-lock loop. *J. Lightw. Technol.*, 29(8):1152–1164, 2011.

[87] Z. Liu, G. Hesketh, B. Kelly, et al. Optical injection-locked directly modulated lasers for dispersion pre-compensated direct-detection transmission. *J. Lightw. Technol.*, 36(20):4967–4974, 2018.

[88] B. Saxberg, B. Plotkin-Swing, and S. Gupta. Active stabilization of a diode laser injection lock. *Rev. Sci. Instrum.*, 87(6), 2016.

[89] C. J. H. Pagett, P. H. Moriya, R. Celistrino Teixeira, et al. Injection locking of a low cost high power laser diode at 461 nm. *Rev. Sci. Instrum.*, 87(5), 2016.

[90] Y. C. Chi, Y. C. Li, H. Y. Wang, et al. Optical 16-qam-52-ofdm transmission at 4 gbit/s by directly modulating a coherently injection-locked colorless laser diode. *Opt. Express*, 20(18):20071–20077, 2012.

[91] Z. Chen, J. Hou, P. Zhou, et al. Mutual injection-locking and coherent combining of two individual fiber lasers. *IEEE J. Quantum Electron.*, 44(6):515–519, 2008.

[92] R. M. Kurtz, R. D. Pradhan, N. Tun, et al. Mutual injection locking: a new architecture for high-power solid-state laser arrays. *IEEE J. Sel. Top. Quantum Electron.*, 11(3):578–586, 2005.

[93] Y. Liu, P. Aashna, Z. Yuan, W. Fu, M. Yang, Y. Yan, L. Qi, M. Zhao, and A. Danner. A lithium niobate cascaded MMI-based arbitrary matrix calculator for convolutional neural networks. *Optics & Laser Technology*, 192:113740, 2025. doi:10.1016/j.optlastec.2025.113740.

[94] Tingting Chen, Beibei Lin, Yeying Jin, Wending Yan, Wei Ye, Yuan Yuan, and Robby T Tan. Dual-rain: Video rain removal using assertive and gentle teachers. In *European Conference on Computer Vision*, pages 127–143. Springer, 2024.

[95] Beibei Lin, Tingting Chen, and Robby T Tan. Geocomplete: Geometry-aware diffusion for reference-driven image completion. *arXiv preprint arXiv:2510.03110*, 2025.

[96] Beibei Lin, Zifeng Yuan, and Tingting Chen. RGB-to-polarization estimation: A new task and benchmark study. In *Advances in Neural Information Processing Systems (NeurIPS)*, 2025. arXiv:2505.13050.

[97] T. Chen, B. Lin, Z. Yuan, Q. Zou, H. He, Y.-S. Ong, A. Goyal, and D. Liu. HypoSpace: Evaluating LLM creativity as set-valued hypothesis generators under underdetermination. In *Proceedings of the 43rd International Conference on Machine Learning (ICML)*, 2026. arXiv:2510.15614.

[98] Tingting Chen, Beibei Lin, Srinivas Anumasa, Vedant Shah, Zifeng Yuan, Qiran Zou, Anirudh Goyal, and Dianbo Liu. Auto-Discovery-Bench: Diagnosing structured state tracking in oracle-guided discovery. *arXiv preprint arXiv:2502.15224*, 2025.

[99] Z. Teng, T. Chen, B. Lin, Z. Yuan, X. Li, X. Zhang, and S. Zhang. RaindropGS: A benchmark for 3D Gaussian splatting under raindrop conditions. *arXiv preprint arXiv:2510.17719*, 2025.

[100] W. Du, Z. Yuan, T. Chen, F. Ke, B. Lin, and S. Zhang. WeatherReasonSeg: A benchmark for weather-aware reasoning segmentation in visual language models. In *European Conference on Computer Vision (ECCV)*, 2026. arXiv:2603.17680.

[101] Beibei Lin, Yeying Jin, Yan Wending, Wei Ye, Yuan Yuan, and Robby T Tan. Nighthaze: Nighttime image dehazing via self-prior learning. In *Proceedings of the AAAI Conference on Artificial Intelligence*, volume 39, pages 5209–5217, 2025.

[102] Beibei Lin, Yeying Jin, Wending Yan, Wei Ye, Yuan Yuan, Shunli Zhang, and Robby T Tan. Nightrain: Nighttime video deraining via adaptive-rain-removal and adaptive-correction. In *Proceedings of the AAAI Conference*

on Artificial Intelligence, volume 38, pages 3378–3385, 2024.